Nodal adsorbate bound states in armchair graphene nanoribbons: Fano resonances and adsorbate recognition in weak disorder

C. H. Chiu and C. S. Chu

Department of Electrophysics, National Chiao Tung University, Hsinchu 30010, Taiwan

(Received 18 September 2014; revised manuscript received 4 November 2014; published 21 November 2014)

We consider adsorbates on metallic armchair-graphene nanoribbons (AGNRs). An adsorbed atom on a nodal site of the gapless subband in the AGNR is found to induce a bound state. The nodal-adsorbate bound state alone does not cause reflection in the AGNR quantum transport in the one propagating-channel regime. Yet its manifestation, as a Fano resonance in G, is brought forth by the presence of a non-nodal adsorbate (or a scatterer) located on a longitudinally separated site. Both the adsorbate-dependent nature and the significantly enhanced energy resolution of the Fano structure in G invite adsorbate recognition. The Fano peak is shown to be robust against weak disorder such as from edge vacancies, due to the localized nature of the Fano resonant state. Adsorbates F and OH, described within an extended Hückel model, are considered as examples.

DOI: 10.1103/PhysRevB.90.195436 PACS number(s): 72.80.Vp, 73.22.Pr, 73.20.Hb, 73.63.−b

I. INTRODUCTION

The novel Dirac properties of graphene [1,2] has prompted much recent research on the quantum transport of graphene nanoribbons (GNRs), both experimentally [3–9] and theoretically [10–23]. One of the spectacular manifestations of the Dirac physics is in the metallic armchair GNRs (AGNRs), where a subband intercepts the Dirac point to become gapless [24]. Disorder effects on the GNR transport have been studied, with disorder due to edge vacancies [11,12,16], edge adsorbates [19], and adsorbates [20,21]. On the other hand, the motivation to tune the GNR energy gap from a microscopic point of view has led to researches on the effects of individual microscopic objects on the GNR. There have been studies of individual doping atoms [13], lattice defects [14,15], vacancies [17,18,22], and adsorbates [19,23] on the quantum transport of GNRs. These single-scatterer studies have found dip structures in G [13–15,17,19,22], whose dip energies are associated with the resonant-state energies due to the scatterer in the GNRs.

Interestingly, for the case of AGNRs, a single dopant [13] or a singe vacancy [17] are found to cause no reflection to the subband when they are located at certain sites of the AGNR. These sites are found to coincide with the nodal sites of the gapless subband in the AGNR [25]. The nodal sites are at transverse coordinate (see Fig. 1) $M = 3m - 1$ for integer m. This is obtained from the transverse profile of the gapless-subband wave function, given by $\sin[k_{nx}a(M+1)]$ (a complete form of the wave function will be presented in Sec. II AII), and from the quantized $k_{nx} = 2\pi/(3a)$ where the Dirac cone is intercepted. Further nodal-type behaviors are found in the AGNR current density profile [14,23], also at the nodal sites of the AGNR. There is no energy in these studies from which one can derive deeper insights about the nodal behavior. Thus far, the nodal behavior has evaded attentions. In this work, we will show that there is indeed a characteristic energy, namely, the nodal-adsorbate bound-state energy, for an adsorbate on a metallic AGNR. The intriguing features of this bound state are explored. Furthermore, its adsorbate-dependent energy is shown appropriate for adsorbate recognition.

Using graphene for adsorbate recognition has been a goal of interest recently. An experimental observation of single gas-molecule adsorption/desorption events had been done on graphene [26]. The basic quanta of charge transfer at the adsorbate site is obtained from the step changes in the Hall resistivity. This charge quanta is used for adsorbate recognition by comparing it with the theoretical calculation results for a number of target adsorbates [27]. Research on the graphene-based gas senors has since been intensive, in both the basic physical aspects [28,29], and the implementation aspects [30]. An alternate adsorbate-recognition scheme of single-adsorbate capability has been proposed recently [31]. This is by way of an optical measurement and with the introduction of a localized state called the localized plasmon resonance (LPR) [32], a collective mode on a patterned two-dimensional nanostructure. Incident lights will undergo diffractive coupling [33] with the LPR to give zero reflection at a wavelength λ_c for a given incident angle [31]. At the zero reflection, the phase of the complex reflection coefficient encounters a singularity, meaning that it is highly sensitive and changes sharply with $\lambda \approx \lambda_c$ [34]. This sharp-change nature in the phase allows a larger phase change to be measured when λ_c is shifted minutely due to the presence of an adsorbate [31].

In this work, we consider quantum transport in metallic AGNR with nodal adsorbates. Our purpose is threefold here. First, we want to show that the nodal sites of the gapless subband have provided us a natural way to obtain localized states. Simply put, the localized state is a bound state induced by an adsorbate located on a nodal site of the gapless subband. As the localized state now carries information about the adsorbate, it plays an even more involved role for the adsorbate recognition here than the LPR states for the optical experiment above. Second, we want to show that the adsorbate bound state provides a significant boost in the energy resolution for the adsorbate recognition. The bound state will manifest as a Fano structure [35] in G, when another adsorbate is located on a longitudinally (along the ribbon) separated non-nodal site of the gapless subband. This Fano structure is robust against weak disorder from random edge vacancies. Third, quantum transport for mesoscopic systems is known to be sensitive to individual scatterers [36] and should thus be so to individual adsorbates.

This paper is organized as follows. In Sec. II, we present our theoretical method for the analysis of the nodal-adsorbate bound state, the nodal-and-non-nodal adsorbate pair, and the

 ©2014 American Physical Society

Green's function for disordered AGNRs. Numerical results and discussions are presented in Sec. III. A conclusion is given in Sec. IV.

II. THEORY

In this section, we consider adsorbate-induced bound and resonant states in metallic AGNRs. Interplay between these states gives rise to adsorbate-dependent Fano resonance in G. Our focus is upon the one-propagating-channel (the gapless subband) regime. The energy of our interest is indicated in Fig. 1 by the $G = 2e^2/h$ region for a pristine AGNR (dotted curve). This energy range, unless explicitly stated otherwise, is the energy for all our following discussions.

A. Nodal-adsorbate bound state

We show here that an adsorbate located on a nodal site of the gapless subband induces a bound state. For W-AGNR of large width W (the number of rows of carbon atoms across the AGNR) the bound-state energy is pinned at the band edge of the AGNR first-gapped subband (FGSB), and is adsorbate independent. For sufficiently narrow W-AGNRs, the bound-state energy moves away from the FGSB's band edge, and becomes adsorbate dependent. Figure 1 is shown first to put things into perspective. A bound state alone does not contribute to the scattering, as is shown in Fig. 1 (the A1-only curve). On the other hand, an adsorbate located on a non-nodal site of the gapless subband induces a resonant state [14,20–22], which alone gives rise to a broad dip structure in G, as is shown in Fig. 1 (the A2-only curve). In the presence of both A1 and A2, a Fano structure is found in G, as is denoted by the black curve in Fig. 1. The Fano peak coincides nicely with the adsorbate-dependent bound-state energy.

The physical picture for the above finding follows naturally from the Lippmann-Schwinger scattering description of the AGNR. The total wave function Ψ, projected onto lattice site

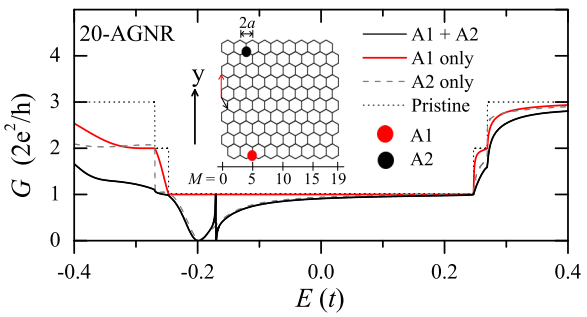

FIG. 1. (Color online) Fano resonances in conductance G of an AGNR with an adsorbate pair A1 and A2. A1 (A2) is a nodal (non-nodal) adsorbate. G's are shown for a pristine AGNR (dotted curve), individual A1 (red curve), A2 (grey dashed curve), and a pair (black curve). Inset is the AGNR (width $W = 20$, along $\hat{x}$, and length along $\hat{y}$) with the scatterers separated by $L = 5$ unit cells along $\hat{y}$. Also indicated are Bravais lattice vectors $\mathbf{A}_1$ (blue arrows), $\mathbf{A}_2$ (red arrows), transverse site-position M, and M-spacing a. The adsorbates are F atoms.

$|j,s\rangle$, given by

$$\Psi_j^s = \phi_j^s + \sum_i G_{jj_i}^{ss_i} V_{j_i} \Psi_{j_i}^{s_i}, \tag{1}$$

is expressed in terms of the lattice-site representation of ϕ, $\hat{G}$, and $\hat{V}$, which are the incident wave function, the AGNR Green's function, and the scatterer on-site potentials, respectively. The lattice sites $|j,s\rangle$ denote the unit-cell coordinates (M_j,N_j), and the sites $s \in \{A,B\}$ within a unit cell. The Bravais lattice point is thus $\mathbf{R}_j = M_j\mathbf{A}_1 + N_j\mathbf{A}_2$, with the Bravais lattice vectors given by $\mathbf{A}_1 = a(\hat{x} - \sqrt{3}\hat{y})$ and $\mathbf{A}_2 = 2\sqrt{3}a\hat{y}$. For an AGNR of width W, we choose $0 \leqslant M_j \leqslant W - 1$. The horizontal distance between two neighboring rows of carbon atoms is $a = 1.23$Å. In this work, we consider W-AGNRs with $W = 3p + 2$ for integer p, which support a gapless subband [24,37,38], when the quantized k_x intercepts the Dirac point.

The standard nearest-neighbor tight-binding model is used for the AGNR, and the adsorbates, located on sites $|j_i,s_i\rangle$, are represented by on-site potentials V_{j_i}. The on-site potential $V_{j_i} = V_a$ of the adsorbate on the site, whose specific form is derived from an extended Hückel model [20]. The extended Hückel model, as described in Ref. [20], has included the extended molecular orbitals α that are formed from the adsorbate-valence orbitals and the carbon atom-valence orbitals (p_z excluded) to which the adsorbate is attached. It results in an energy-dependent on-site potential V_a, of the form

$$V_a = t \sum_\alpha \frac{|\gamma_\alpha|^2}{E - \varepsilon_\alpha}, \tag{2}$$

where $t = 2.66$ eV is the hopping coefficient of graphene. The values of the adsorbate parameters γ_α and ε_α have been obtained by Ihnatsenka *et al.* [20]. For completeness, we list the parameters for adsorbates F and OH in Table I

For the case of a single nodal adsorbate, the condition for the induction of a bound state is derived from Eq. (1), by setting $\phi = 0$, to give

$$\left[1 - G_{j_1j_1}^{s_1s_1}(E)\, V_a\right] \Psi_{j_1}^{s_1} = 0. \tag{3}$$

That the bound state can be found is facilitated by $G_{j_1j_1}^{s_1s_1}(E)$ becoming a real function of E when j_1 is a nodal site of the gapless subband. This is clearly shown in a subband-index (n) summation form of $G_{jj'}^{ss'}(E)$.

From $G_{jj'}^{ss'}(E) = \langle js|\hat{G}(E)|j's'\rangle$, where $\hat{G}(E) = (E - \hat{H} + i\eta)^{-1}$ is the retarded Green's function, and $\hat{H}$ the

TABLE I. Parameters for adsorbate F and OH obtained by Ihnatsenka *et al.* in Ref. [20].

Adsorbate	$\epsilon_\alpha(t)$	$\gamma_\alpha(t)$
F	−10.862	4.363
	−2.460	1.645
	−0.914	1.180
OH	−8.536	3.203
	−1.802	1.779
	−0.709	1.540

Hamiltonian of a pristine AGNR, we have

$$G^{ss'}_{jj'}(E) = \sum_{\mathbf{k}_n,\,\nu} \langle js|\mathbf{k}_n,\nu\rangle \frac{1}{E-\nu E_{\mathbf{k}_n}+i\eta} \langle \mathbf{k}_n,\nu|j's'\rangle, \quad (4)$$

of which $\nu E_{\mathbf{k}_n}$ is the graphene dispersion relation, $\nu = \pm 1$, $\mathbf{k}_n = (k_{nx},k_y)$, and η is a positive quantity of infinitesimal magnitude. The subband wave function is given by

$$\langle js|\mathbf{k}_n,\nu\rangle = \sqrt{\frac{2}{(W+1)N_y}}\, e^{ik_y\sqrt{3}a(2N_j-M_j)} \times \sin\left[k_{nx}a(M_j+1)\right] C^{s}_{\mathbf{k}_n\nu}, \quad (5)$$

where N_y denotes the total number of unit cells along the AGNR, $(C^{A}_{\mathbf{k}_n\nu}, C^{B}_{\mathbf{k}_n\nu})^T = \frac{1}{\sqrt{2}}(1,\nu H^{*}_{\mathbf{k}_n}/|H_{\mathbf{k}_n}|)^T$ is the normalized pseudospinor [39], with $H_{\mathbf{k}_n} = -t\,[1 + 2e^{-i\sqrt{3}k_y a}\cos(k_{nx}a)]$, and $E_{\mathbf{k}} = |H(\mathbf{k})|$.

Simplifying Eq. (4) leads to a useful subband-index summation form of $G^{ss'}_{jj'}$, given by

$$G^{ss'}_{jj'}(E) = \frac{\sqrt{3}a}{2\pi\,(W+1)} \sum_n F^n_{jj'}\, g^n_{jj',ss'}(E), \quad (6)$$

where $g^n_{jj',ss'}(E)$ is the reduced Green's function,

$$g^n_{jj',ss'}(E) = \sum_\nu \int_{-\pi/\sqrt{3}a}^{\pi/\sqrt{3}a} dk_y \frac{e^{ik_y\sqrt{3}a\,L_{jj'}}\, C^{s*}_{\mathbf{k}_n\nu} C^{s'}_{\mathbf{k}_n\nu}}{E-\nu E_{\mathbf{k}_n}+i\eta}. \quad (7)$$

The factor in the summation of Eq. (6),

$$F^n_{jj'} = 4\sin[k_{nx}(M_j+1)a]\sin[k_{nx}(M_{j'}+1)a], \quad (8)$$

is associated with the nth subband's transverse profile, and is zero when j or j' are at a nodal site. In Eq. (7), $L_{jj'} = (R_{jy} - R_{j'y})/\sqrt{3}a$ is the longitudinal distance between the Bravais lattice points j and j'. The subband index ranges $1 \leqslant n \leqslant \lceil W/2 \rceil$ such that $k_{nx} = \frac{\pi}{a(W+1)}(\lfloor W/2 \rfloor + n)$, where $\lfloor x \rfloor$ ($\lceil x \rceil$) denotes the largest (smallest) integer not greater (less) than x.

The same-site reduced Green's function $g^n_{jj,ss}(E)$ is a real (complex) function of E when E lies outside (inside) of the nth subband. This is seen from applying the Cauchy principal-value analysis to Eq. (7). Consequently, within our energy range of interest, a nodal adsorbate will shunt the only term of $G^{ss}_{jj}(E)$ in Eq. (6) that is complex—the term from the gapless subband. The nodal-bound state is hence orthogonal to the gapless subband, and does not cause reflection to the gapless subband, leaving $G = 2e^2/h$ in our energy of interest. Its wave function is given by

$$\Psi^s_j = V_{\rm a}\, G^{ss_1}_{jj_1}\, \Psi^{s_1}_{j_1}, \quad (9)$$

with the energy fixed at the bound-state energy $E_{\rm B}$, and $\Psi^{s_1}_{j_1}$ fixed by the normalization.

A non-nodal adsorbate, following a similar argument, will have retained in $G^{ss}_{jj}(E)$ the term from the gapless subband such that $G^{ss}_{jj}(E)$ becomes complex. The non-nodal adsorbate cannot then form a bound state, since the condition Eq. (3) does not hold, but forms a resonant state instead. The resonant condition is given by

$$1 - V_{\rm a}\,{\rm Re}\left[G^{s_1s_1}_{j_1j_1}(E)\right] = 0. \quad (10)$$

B. *N* Nodal adsorbates and one non-nodal adsorbate

Coherent interplay between the bound and resonant states gives rise to a Fano resonance in G. Taking the point of view that a non-nodal adsorbate plays the role of revealing the adsorbate-induced bound states in the AGNR, we consider in this subsection first a nodal and a non-nodal adsorbate pair. Then we consider N nodal adsorbates and one non-nodal adsorbate.

For an adsorbate pair consisting of a nodal (A1) and a non-nodal (A2) adsorbate, the Fano peak in G occurs exactly at the bound-state energy, and with $G = 2e^2/h$. This is most easily seen from projecting Eq. (1) onto the lattice sites of A1 and A2, to give

$$\begin{pmatrix} 1 - V_{\rm a}\, G^{s_1s_1}_{j_1j_1} & -V_{\rm a}\, G^{s_1s_2}_{j_1j_2} \\ -V_{\rm a}\, G^{s_2s_1}_{j_2j_1} & 1 - V_{\rm a}\, G^{s_2s_2}_{j_2j_2} \end{pmatrix} \begin{pmatrix} \Psi^{s_1}_{j_1} \\ \Psi^{s_2}_{j_2} \end{pmatrix} = \begin{pmatrix} \phi^{s_1}_{j_1} \\ \phi^{s_2}_{j_2} \end{pmatrix}. \quad (11)$$

The $\phi^{s_1}_{j_1} = 0$ for the incident wave function at A1 leads to the important result

$$\Psi^{s_2}_{j_2} = 0, \quad (12)$$

when the incident energy is at the A1's bound-state energy, where Eq. (2) holds. That the total scattering wave function $\Psi^{s_2}_{j_2}$ vanishes (note: not the total scattering wave function $\Psi^{s_1}_{j_1}$ at the site of A1) is a result of the no-damping nature of the A1-induced bound state. The total wave function Ψ^s_j, according to Eq. (1), becomes

$$\Psi^s_j = \phi^s_j + V_{\rm a}\, G^{ss_1}_{jj_1}\, \Psi^{s_1}_{j_1}. \quad (13)$$

The second term (scattered wave) in Eq. (13) is shown, in the following, to be evanescent waves, and does not contribute to the current. Thus we have perfect transmission ($G = 2e^2/h$) at the Fano peak whose energy is at $E_{\rm B}$.

The reduced Green's function $g^n_{jj',ss'}(E)$ is calculated by both numerical and analytical methods. Excellent consistent results are obtained. Analytical results shed light on our understanding of the physics. The characteristics of the reduced Green's function are best illustrated by the analytic expression ($s = s'$ case) we obtained below via explicit calculations of the integral in Eq. (7) [40]. The calculation is facilitated by the canceling of a branch-cut integral through the ν summation in Eq. (7). We get

$$g^n_{jj',ss}(E) = -\xi^n_E \frac{\pi}{4\sqrt{3}\,at^2} \frac{E}{\beta_n} \frac{e^{-\xi^n_E\sqrt{3}\,\Delta_{jj'}\,\kappa_{ny}\,a}}{\sinh(\sqrt{3}\,\kappa_{ny}\,a)}, \quad (14)$$

for a non-flat-band subband, where $\Delta_{jj'} = |L_{jj'}|$. For a flat-band subband (the $n = 1$ subband when W is odd), we have

$$g^1_{jj',ss}(E) = \frac{2\pi}{\sqrt{3}\,a} \frac{E}{E^2 - t^2 + 2iE\eta}\, \delta_{jj'}. \quad (15)$$

Here

$$\kappa_{ny} = \frac{1}{\sqrt{3}\,a} \ln(\Gamma_n + \sqrt{\Gamma_n^2 - 1}), \quad (16)$$

where $\Gamma_n = \beta_n + [1 - (E/t)^2]/(4\beta_n)$, and $\beta_n = -\cos(k_{nx}\,a)$.

When E lies outside of the nth subband, $\xi^n_E = 1$ and κ_{ny} is real, we have an evanescent nature in $g^n_{jj',ss}(E)$. When E lies inside the nth subband, $\xi^n_E = -{\rm sgn}(E)$ and κ_{ny} is complex,

then $g^n_{jj',ss}(E)$ is of a propagating-wave nature. These features also lead to our finding that the coupling between the bound and the resonant states, represented by the off-diagonal terms in Eq. (11), decreases with increasing $\Delta_{j_1 j_2}$ exponentially.

Remarkably, for configurations that involve N nodal adsorbates and a non-nodal adsorbate, the Fano-peak conductances still manage to maintain their $G = 2e^2/h$ value. Following our analysis in Eq. (11) and Eq. (13), but for N nodal adsorbates, the vanishing of the total scattering wave function $\Psi_{N+1} \equiv \Psi^{s_{N+1}}_{j_{N+1}} = 0$ at the $(N+1)$th adsorbate, that is, the non-nodal adsorbate, can be achieved. It is given by the condition

$$\det \mathbf{Q}(E) = 0. \tag{17}$$

Matrix elements of $\mathbf{Q}$ are given by

$$Q_{ii'} = \begin{cases} 1 - V_{\rm a} G_{ii}, & i = i', \\ -V_{\rm a} G_{ii'}, & i \neq i'. \end{cases} \tag{18}$$

Here subscripts i and i' denote the nodal adsorbates. To keep notations simple, we define $G_{ii'} \equiv G^{s_i s_{i'}}_{j_i j_{i'}}$.

The useful relation $G_{ii'} = G^*_{i'i}$ is obtained from the transformation properties of $E(\mathbf{k})$ and $C^s_{\mathbf{k}_n \nu}$ when k_y changes sign. That $Q_{ii'}$ is, in fact, real results from $C^A_{\mathbf{k}_n \mu}$ being real. These properties of $\mathbf{Q}$ lead to a real equation in Eq. (17); the energies it gives correspond to the Fano peak energies, and should also correspond to the bound-state energies of the N nodal-adsorbate configurations. The exponential behavior of $G_{ii'}$ for $i \neq i'$ helps to suppress the energy shift of these Fano peaks from the adsorbate bound-state energies of the individual nodal adsorbate.

C. Green's function $\hat{\tilde{G}}$ for disordered AGNRs

The AGNR Green's function $\hat{\tilde{G}}$ in the presence of vacancies is given by the relation

$$\hat{\tilde{G}} = \hat{G} + \hat{G}\hat{V}\hat{\tilde{G}} = \hat{G} + V_0 \hat{G}\ \hat{I}_{\rm v}\ \hat{\tilde{G}}, \tag{19}$$

where $\hat{G}$ is the Green's function for the pristine AGNR. The vacancy potential $\hat{V} \equiv V_0\ \hat{I}_{\rm v} = V_0 \sum_{i'} |i'\rangle\langle i'|$, where $\hat{I}_{\rm v}$ is the projection operator into $\{|i'\rangle\}$, the subspace spanned by the vacancy lattice sites. Here V_0 is the vacancy on-site potential, which will be set to infinity at the end of the derivation. The derivation in this subsection becomes that for edge vacancies when their lattice sites are at the edge sites of the AGNR.

Applying the projection operator $\hat{I}_{\rm v}$ from the left to Eq. (19), we get

$$\hat{I}_{\rm v}\ \hat{\tilde{G}} = \hat{I}_{\rm v}\ \hat{G} + V_0\ \hat{I}_{\rm v}\ \hat{G}\ \hat{I}_{\rm v}\ \hat{\tilde{G}}.$$

After rearranging terms, we obtain

$$\hat{I}_{\rm v}\ \hat{\tilde{G}} = [\hat{I}_{\rm v} - V_0\ \hat{I}_{\rm v}\ \hat{G}\ \hat{I}_{\rm v}]^{-1} \hat{I}_{\rm v}\ \hat{G}. \tag{20}$$

We substitute Eq. (20) into Eq. (19) to get

$$\hat{\tilde{G}} = \hat{G} + V_0 \hat{G}\ \hat{I}_{\rm v}[\ \hat{I}_{\rm v} - V_0\ \hat{I}_{\rm v}\ \hat{G}\ \hat{I}_{\rm v}]^{-1} \hat{I}_{\rm v}\ \hat{G}. \tag{21}$$

Finally, taking the $V_0 \to \infty$ limit, we arrive at

$$\hat{\tilde{G}} = \hat{G} - \hat{G}\ \hat{I}_{\rm v}[\ \hat{I}_{\rm v}\ \hat{G}\ \hat{I}_{\rm v}\ ]^{-1}\ \hat{I}_{\rm v}\ \hat{G}. \tag{22}$$

The expression for the one-vacancy case of Eq. (22) is the same as in Ref. [41].

Our results also check with the expectation that the eigenstates $\tilde{\phi}$ in the presence of the vacancies should vanish at their respective lattice sites. This expected condition $\hat{I}_{\rm v}\tilde{\phi} = \tilde{\phi}^\dagger \hat{I}_{\rm v} = 0$ is satisfied by applying $\hat{I}_{\rm v}$ to Eq. (22) to get

$$\hat{I}_{\rm v}\ \hat{\tilde{G}} = \hat{\tilde{G}}\ \hat{I}_{\rm v} = 0.$$

The eigenstates $\tilde{\phi}$ and their counterparts ϕ for the pristine AGNR are connected by the relation $\tilde{\phi} = \phi + \hat{G}\ V_0\ \hat{I}_{\rm v}\ \tilde{\phi}$. The relation is reexpressed in the form

$$\tilde{\phi} = \phi - \hat{G}\ \hat{I}_{\rm v}[\ \hat{I}_{\rm v}\ \hat{G}\ \hat{I}_{\rm v}\ ]^{-1}\ \hat{I}_{\rm v}\ \phi. \tag{23}$$

Building on the above relations for the treatment of the edge vacancies, we consider the case of an adsorbate pair with the edge vacancies in the background. The adsorbate pair consists of a nodal (A1) and a non-nodal (A2) adsorbates. The total scattering wave function $\tilde{\Psi}$ resulted from an incident wave $\tilde{\phi}$ is given by

$$\tilde{\Psi}^s_j = \tilde{\phi}^s_j + V_a \tilde{G}^{s s_1}_{j j_1} \tilde{\Psi}^{s_1}_{j_1} + V_a \tilde{G}^{s s_2}_{j j_2} \tilde{\Psi}^{s_2}_{j_2}. \tag{24}$$

Projecting $\tilde{\Psi}$ at the adsorbate lattice sites, we obtain a similar equation as in Eq. (11), given by

$$\begin{pmatrix} 1 - V_{\rm a}\,\tilde{G}^{s_1 s_1}_{j_1 j_1} & -V_{\rm a}\,\tilde{G}^{s_1 s_2}_{j_1 j_2} \\ -V_{\rm a}\,\tilde{G}^{s_2 s_1}_{j_2 j_1} & 1 - V_{\rm a}\,\tilde{G}^{s_2 s_2}_{j_2 j_2} \end{pmatrix} \begin{pmatrix} \tilde{\Psi}^{s_1}_{j_1} \\ \tilde{\Psi}^{s_2}_{j_2} \end{pmatrix} = \begin{pmatrix} \tilde{\phi}^{s_1}_{j_1} \\ \tilde{\phi}^{s_2}_{j_2} \end{pmatrix}. \tag{25}$$

In the weak disorder regime, when the density of the edge vacancy is low, the nodal physics and its evanescent effects will play a crucial role. The evanescent effects are exerted via G_{1i} or G_{i1}, where i denotes the edge-vacancy lattice sites. In the following, we will trace these evanescent effects in several physical quantities of interest for the elucidation of the evanescent effects on the Fano structures.

The incident wave function $\tilde{\phi}^{s_1}_1$ is found to take on the form $\tilde{\phi}^{s_1}_1 = \delta\tilde{\phi}^{{\rm evan},s_1}_1$ from projecting Eq. (23) to the nodal site A1. The superscript in $\delta\tilde{\phi}^{{\rm evan},s_1}_1$ indicates that the term is of evanescent nature (between A1 and the edge vacancies) and is small when evanescent suppression prevails. Since $\phi^{s_1}_1 = 0$, the G_{1i} factor in the scattering term of Eq. (23) brings about the evanescent effects to $\tilde{\phi}^{s_1}_1$.

For $\hat{\tilde{G}}$, or its matrix element $\tilde{G}_{j1}$, the second term in Eq. (22) contains G_{i1} such that $\tilde{G}_{j1}$ should be cast in the form

$$\tilde{G}_{j1} = G_{j1} + \delta\tilde{G}^{\rm evan}_{j1}, \tag{26}$$

where j denotes a general lattice site. Furthermore, for the $j = 1$ case, the second term of Eq. (26) is of even higher order in the evanescent effects. Finally, for the Fano structure, we consider Eq. (25). At around the Fano peak energy $E_{\rm B}$, we have the equation

$$-V_{\rm a}\,\delta\tilde{G}^{\rm evan}_{11}\,\tilde{\Psi}^{s_1}_1 - V_{\rm a}\,\tilde{G}_{12}\,\tilde{\Psi}^{s_2}_2 = \delta\tilde{\phi}^{{\rm evan},s_1}_1, \tag{27}$$

from which we conclude for $\tilde{\Psi}^{s_2}_2$ the form $\tilde{\Psi}^{s_2}_2 = \delta\tilde{\Psi}^{{\rm evan},s_2}_2$. Putting all these together, the total scattering wave function in Eq. (24) becomes

$$\tilde{\Psi}^s_l = \tilde{\phi}^s_l + V_a\big[G_{l1} + \delta\tilde{G}^{\rm evan}_{l1}\big]\,\tilde{\Psi}^{s_1}_1 + V_a\tilde{G}_{l2}\,\delta\tilde{\Psi}^{{\rm evan},s_2}_2. \tag{28}$$

The term involving G_{l1} is an evanescent wave and does not contribute to G. The last two terms in Eq. (28) consist of the propagating channel but suffer suppression from the evanescent effects. Thus, in the vicinity of $E_{\rm B}$, the conductance

G is basically that determined by $\tilde{\phi}$. In other words, the Fano peak will rise to the conductance as is determined by the background edge vacancies. The shift in the Fano-peak energy is also small, being protected by the evanescent effects. These features are confirmed in our numerical results.

III. RESULTS

Numerical examples presented in this section aim at the illustration of three major points. The first point is the nodal-adsorbate bound states. The second is the adsorbate recognition from using the bound states. And the third is the robustness of the adsorbate recognition against weak disorder.

A. Nodal-adsorbate bound states

The nodal-adsorbate-induced bound state in metallic AGNRs is presented in this subsection. Taking a 20-AGNR as an example, the nodal sites are at $M = 2$, 5, and 8, which are equivalent to nodal sites at $M = 17$, 14, and 11, respectively. For the case when the adsorbate is F, their bound-state energies are $-0.209t$, $-0.171t$, and $-0.159t$, corresponding sequentially to the nodal sites listed earlier. As a reference, the first-gapped subband band edge is at $-0.25t$.

Key features we present include the nodal-adsorbate bound-state wave functions, their Fano structures in G by a neighboring non-nodal adsorbate, the localized (or evanescent) nature of the bound state, and the bound states that are formed from a few nodal adsorbates.

Figure 2 presents (a) the wave function Ψ and (b) the $|\Psi|^2$. Equation (9) is used for this purpose. The adsorbates F are located on nodal sites $M = 17$ (a); 5 (b); and 8 (c). The fact that Ψ is real, according to the discussion in the paragraph just after Eq. (18), allows us to make the Ψ plot as it is. The positions of the nodal adsorbate are at the centers of the yellow triangular structures in the Ψ contours. Similar triangular structures have been obtained, but in the local density of states at zero energies around a vacancy in bulk graphene [41,42]. For the sake of our following discussions, we denote the nodal-adsorbate site to be an A site. Its nearest neighboring site along the ribbon direction is the B site in the same unit cell. The $|\Psi|^2$ contour in Fig. 2 (lower figures) shows that $|\Psi|^2$ weights more, in general, on the B site. This trend is in agreement with that for a vacancy [41]. The very large on-site potential V_0 for the vacancy has pushed the wave function of its zero-energy state to the B (A) site entirely when the vacancy is at an A (B) site.

Another trend of interest that holds better for the more central-nodal adsorbate ($M = 8$) is related to the asymmetric, or symmetric, weighting of the $|\Psi|^2$ for the A, B sites in a unit cell. This weighting feature depends on the longitudinal displacement of the unit cell of interest from the nodal adsorbate. In Fig. 2, asymmetric (symmetric) weighting of $|\Psi|^2$ occurs when the unit cell is on the smaller (larger) y-coordinate side of the nodal adsorbate. The origin of this is that $|\Psi|^2$ for A sites exhibit a $\pi/3$ symmetry (with a $y \to -y$ symmetry) while that for B sites exhibit a $2\pi/3$ symmetry (without a $y \to -y$ symmetry). The A-, B-site correlations in the above conclusion will switch accordingly if the nodal adsorbate is switched to a B site. It is because of the A, B site symmetry in the AGNR. When the nodal adsorbate is close to the AGNR edge ($M = 17$), the second trend is greatly disrupted. Similarly, looking at the central-nodal adsorbate in the Ψ-contour plot, Fig. 2(c) (upper figure), we see that the three lines of A-B sites leading outward from

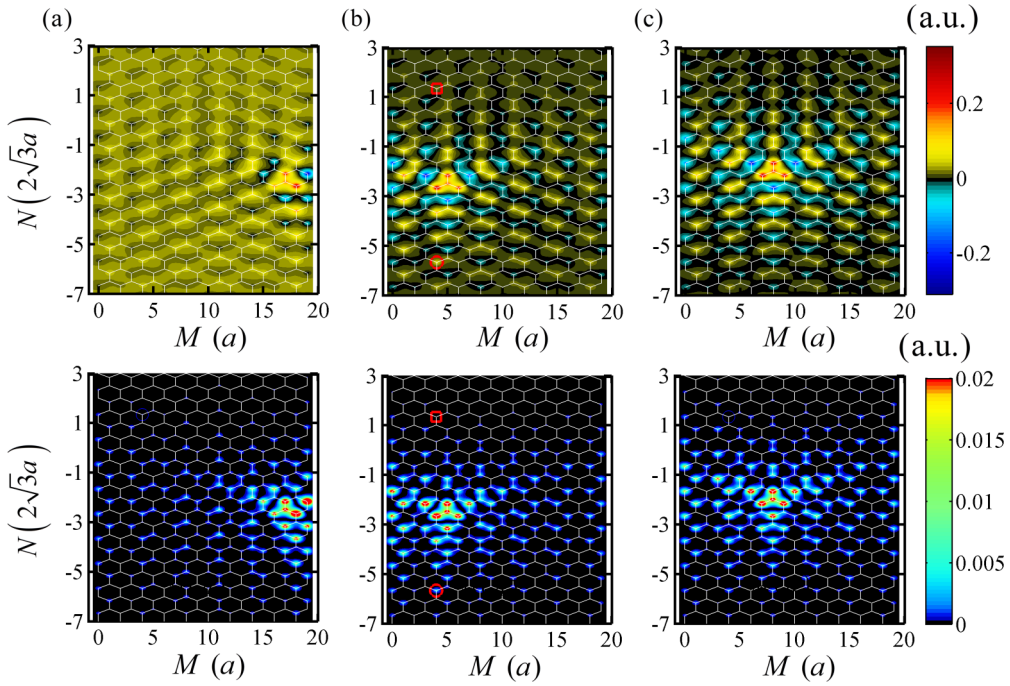

FIG. 2. (Color online) Nodal-adsorbate bound-state wave functions Ψ (upper figures) and $|\Psi|^2$ (lower figures). Adsorbates at nodal sites $M = 17$, 5, and 8 are presented in (a)–(c), respectively. The adsorbate is F. The sites in (b) marked by grey (red) open symbols are B sites to be attached upon by non-nodal adsorbates in Fig. 3. For display purpose, s-like functions are used in place of the site orbitals.

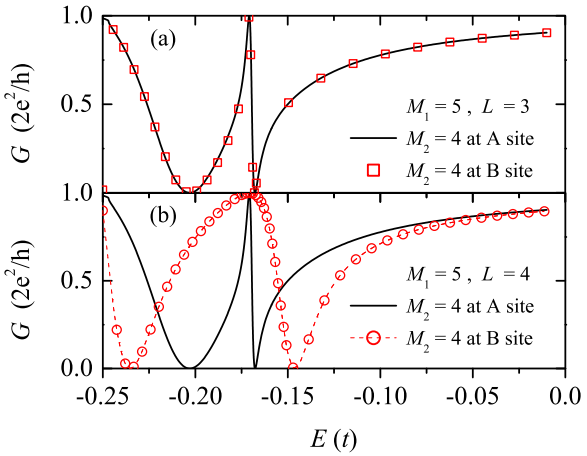

FIG. 3. (Color online) A-, B-site symmetry (asymmetry) in Fano structures for adsorbate pairs. Adsorbate pair in Fig. 2(b) with the non-nodal adsorbate located on a site of the A-B unit cell denoted by (a) grey (red) open square, and (b) grey (red) open circle. Solid (black) curves are for non-nodal adsorbate located on the A site, and open (red) symbols are for non-nodal adsorbate located on the B site.

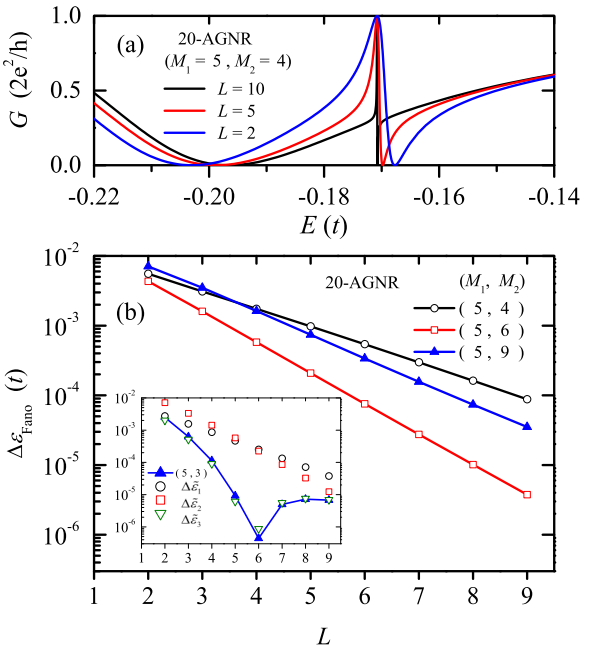

FIG. 4. (Color online) Fano structures and Fano widths vs separation L in an adsorbate pair. (a) Conductance G for $L = 10, 5$, and 2, in units of $2\sqrt{3}a$. (b) Exponential-type dependence of the Fano width $\Delta\varepsilon_{\rm Fano}$, the peak-dip energy difference, on L for non-nodal adsorbate at $M = 4$, 6, and 9. Inset (solid curve) is for non-nodal adsorbate at $M = 3$.

the three vertices of the yellow triangle have Ψ exhibiting monotonically decreasing characteristics. On the other hand, the three directions leading outward from the three bases of the yellow triangle have Ψ exhibiting oscillatory decaying characteristics. These characteristics should be of interest for exploring interactions between nodal adsorbates.

The asymmetric (symmetric) weighting of $|\Psi|^2$ in a unit cell is reflected in Fig. 3, via the Fano structure in G, when a non-nodal adsorbate is in the neighborhood. The nodal adsorbate is the one in Fig. 2(b). The unit-cell locations of the non-nodal adsorbates for the adsorbate pair are denoted by grey (red) open symbols in Fig. 2(b). The symmetric weighting case, Fig. 3(a), occurs when the non-nodal adsorbate is located on the larger y-coordinate side of the nodal adsorbate. It is illustrated by the almost complete overlapping in the Fano structures in Fig. 3(a). The solid black curve and the red open symbols denote the case of an A- and B-site non-nodal adsorbate, respectively. On the other hand, the asymmetric weighting case, Fig. 3(b), occurs when the non-nodal adsorbate is located on the smaller y coordinate side of the nodal adsorbate. It is illustrated by the very different Fano-structure widths in Fig. 3(b). Again, the solid black curve and the red open symbols denote the case of an A- and B-site non-nodal adsorbate, respectively. Note that both of the dip structures in G experience quite a significant relative energy shift ($\approx 0.025t$) between the two G curves. In contrast, that the Fano-peak energy shows no relative energy shift, and the Fano-peak G remains at $2e^2/h$ is in excellent accord with our analysis leading up to Eq. (17). Since these two key features of our focus in this work remain intact, regardless of whether the adsorbate pair belongs to AA type or AB type, we will assume only AA-type adsorbate-pair configurations in the following examples for the sake of focusing our presentations on the essentials.

The robustness in the Fano peak is due to the localized nature of the bound state. This is shown in Fig. 4, when the L dependencies of the Fano structure in G and the Fano width are presented in Figs. 4(a) and 4(b), respectively. As the longitudinal separation L decreases, from $L = 10$, 5, to 2, the Fano peaks in Fig. 4(a) show broadening peak-and-dip structures, while the Fano-peak energy and G remain unchanged. Here L is in units of $2\sqrt{3}a$. A more systematic study is shown in Fig. 4(b), when the L dependence of the Fano width $\Delta\varepsilon_{\rm Fano}$ is presented. The Fano-peak width $\Delta\varepsilon_{\rm Fano}$ is defined as the Fano peak-dip energy difference. For the same nodal adsorbate, we present curves from different non-nodal adsorbates ($M = 3$,4,6,9). The cases for $M = 4$, 6, 9 show exponential dependence of $\Delta\varepsilon_{\rm Fano}$ on L. The case for $M = 3$, shown in the inset of Fig. 4(b), seems to need further exploration below. It turns out, as is shown in Fig. 1 (dotted curve), that the band edge of the first and second gapped subbands contribute comparably to the exponential behavior, because of their proximity in energy to the bound state. Our analysis shows that these two exponential contributions come to a cancellation at a certain L, leading to the seemingly nonexponential dependence on L. An explicit exposition of this understanding is by artificial keeping in $\hat{G}$ only the first-gapped subband (the $\Delta\tilde{\varepsilon}_1$ curve), or only the second-gapped subband (the $\Delta\tilde{\varepsilon}_2$ curve), or only both (the $\Delta\tilde{\varepsilon}_3$ curve), and compare with the full numerical calculation (full curve), as is nicely presented in Fig. 4(b) (inset). The exponential or evanescent nature behind the Fano structures is thus established.

Fano characteristics for adsorbate configurations involving more than one nodal adsorbates are presented in Fig. 5. The implication on the bound states is our focus here. Specifically, we consider the $N = 3$ case, where indicated in the inset are the nodal-adsorbate positions (red solid circles) and the

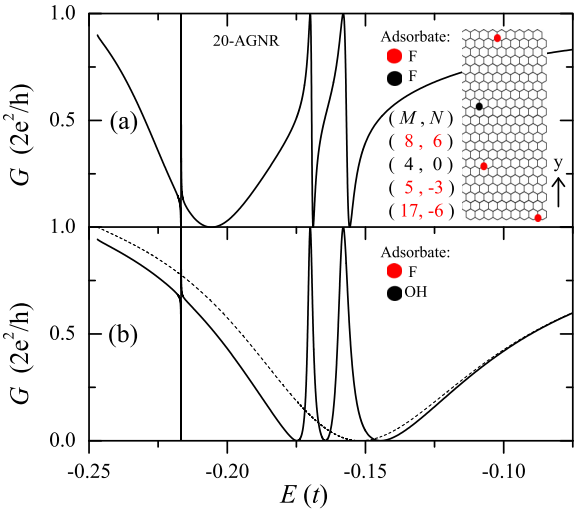

FIG. 5. (Color online) G for three nodal adsorbates and one non-nodal adsorbate. Lattice sites (M,N) are (8,6), (5,−3), and (17,−6) for the nodal adsorbates, and (4,0) for the non-nodal adsorbate. All adsorbates are F in (a), and the non-nodal adsorbate is changed to OH in (b).

non-nodal adsorbate position (black solid circle). The non-nodal adsorbate plays the role of revealing the bound states. Figure 5(a) shows that there are three Fano structures. The fact that these Fano peaks all have $G = 2e^2/h$ shows, according to our analysis following Eq. (17), that the Fano-peak energies correspond to bound states. These bound-state energies are at $-0.216t$, $-0.169t$, and $-0.158t$, which are pretty close to the bound-state energies for individual nodal adsorbate, at $M = 17$, 5, and 8, respectively, given in the beginning of this subsection. In terms of percentage-energy shifts, they are -3.2%, $+1.2\%$, and $+0.6\%$. The signs of these percentage-energy shifts are consistent with level repulsion. The $M = 17$ bound-state level has a greatest percentage-energy shift due to the proximity of the $M = 17$ to the $M = 5$ adsorbates. The Fano width of the $M = 17$ is narrowest because of the farthest distance the associated nodal adsorbate is separated from the non-nodal adsorbate. To illustrate that the results are robust against the type of non-nodal adsorbate, we show in Fig. 5(b) the case when the non-nodal adsorbate becomes OH. For reference, we also plot in Fig. 5(b) the G (dotted curve) for a single OH. In summary, the exponential nature of the nodal bound states has kept intact the Fano-peak energies and G values.

B. Adsorbate recognition

The key feature we present here is the adsorbate-recognition capability provided by the adsorbate-dependent bound states. For comparison, we use both F and OH as adsorbates. For illustration, we have included three metallic AGNR of different widths.

Presented in Figs. 6(d) and 6(e) are Fano peaks of adsorbate pairs from adsorbate species F and OH, respectively, and for 20-AGNR. The Fano-peak energy spectrum is clearly distinct for the two adsorbate species. In contrast to the broad dip of the adsorbate resonant state, the Fano profile has significantly enhanced the energy resolution. Adsorbate recognition is

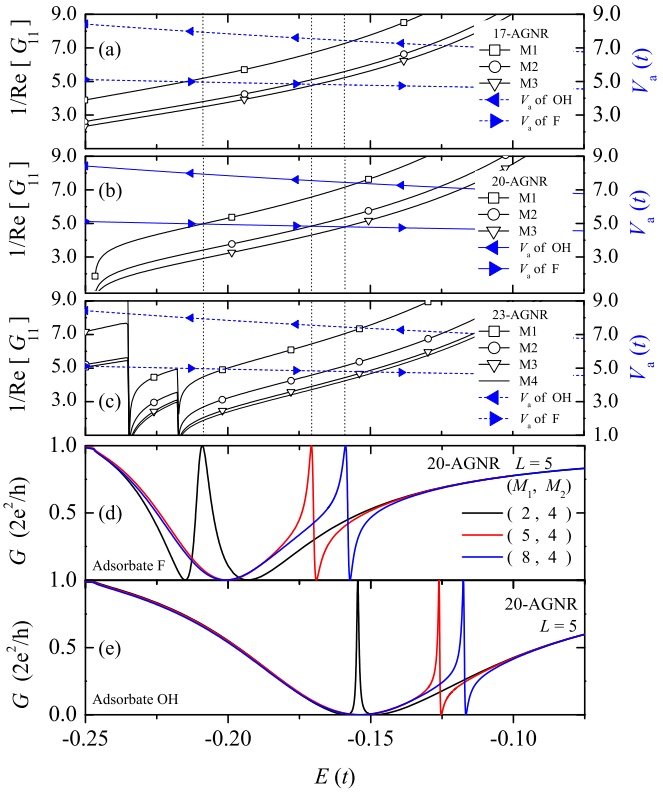

FIG. 6. (Color online) *Look-up figures* for adsorbate recognition. (a)–(c) are *look-up figures* for AGNR of $W = 17$, 20, and 23, respectively. V_a curves for adsorbate OH (F) are denoted by solid left- (right-)pointing triangles with V_a referring to the right-ordinate scale. $1/\mathrm{Re}\,[G_{11}]$ curves for W-AGNR at nodal sites MI are denoted by open symbols. G curves in (d) and (e) denote adsorbate pairs (L, M_1, and M_2) for F and OH, respectively. Vertical dotted lines in (a)–(c) are guides to adsorbate recognition for (d).

facilitated by *look-up-figures*, as in Figs. 6(a)–6(c). Here $1/[G_{11}]$ (which is also $1/\mathrm{Re}\,[G_{11}]$ in the energy range of our interest) intercepts V_a to produce the adsorbate bound-state energies. Each nodal site MI, the Ith nodal site counted from a ribbon edge, contributes a $1/\mathrm{Re}\,[G_{11}]$ curve. These curves, as shown in Figs. 6(a)– 6(c) for $W = 17$, 20, and 23, respectively, serve to identify the adsorbate represented by, for instance, the Fano peaks in Fig. 6(d). Guided by the three vertical dotted lines, we see that OH is clearly out of the consideration, and F fits best for the $W = 20$ case in Fig. 6(b). Furthermore, both the $W = 23$ and 17 cases can be ruled out when the entire Fano-peak spectrum is utilized. Thus our scheme could also provide us information about W. The boasting of the energy resolution by the Fano structures, in contrast to the energy resolution provided by the width of the resonant state, has made possible the above adsorbate recognition scheme.

C. Robustness of our adsorbate recognition against weak disorder

The robustness of the Fano structures as well as the adsorbate recognition capability against weak disorder is illustrated. The disorder is provided by edge vacancies. We have performed the ensemble average of G over disorder

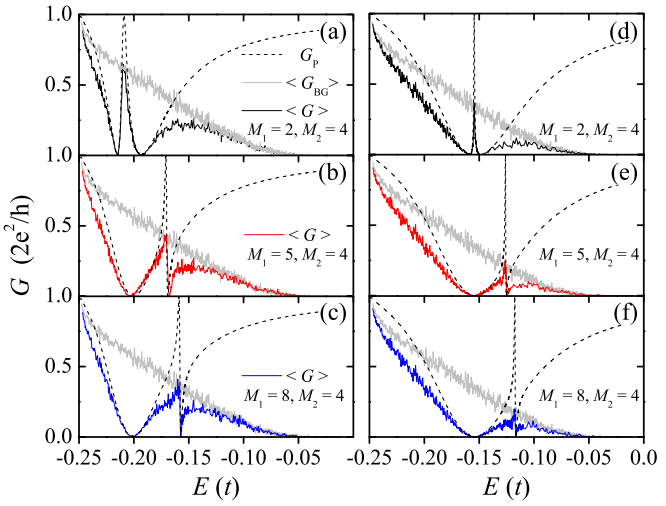

FIG. 7. (Color online) Effects of disorder due to edge vacancies on the Fano resonance of an adsorbate pair from F (a)–(c) and OH (d)–(f). The adsorbates are at M_1 and M_2 with separation $L = 5$ along a 20-AGNR. Conductance curves G_p (dashed curves) are for an adsorbate pair only, $\langle G_{BG} \rangle$ (grey curves) are for edge-vacancy disorder only, and $\langle G \rangle$ (solid curves) are for both the adsorbate pair and edge-vacancy disorder. The edge vacancies distribute over $L_0 \sim 1\ \mu$m with concentration $P_v = 0.125\%$. Average conductance $\langle G \rangle$ is obtained for 100 disorder samples.

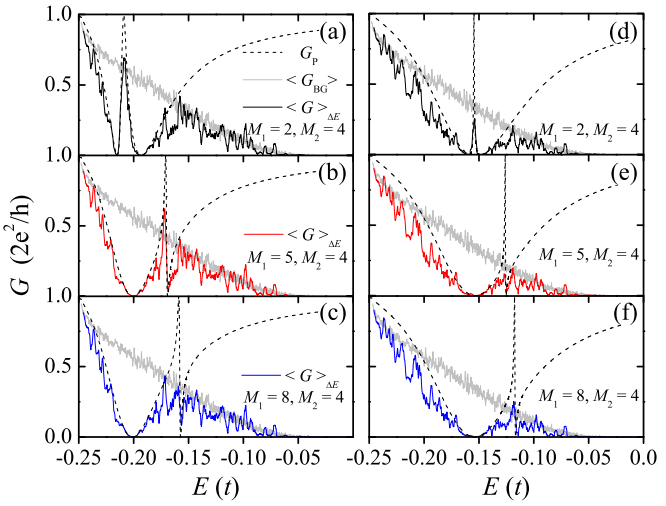

FIG. 8. (Color online) Same plot as in Fig. 7 except that the number of edge-vacancy configurations is 3. The adsorbates are at M_1 and M_2 with separation $L = 5$ along a 20-AGNR. Adsorbate pair is from F (a)–(c) and OH (d)–(f). Conductance curves G_p (dashed curves) are for an adsorbate pair only, and $\langle G_{BG} \rangle$ (grey curves) are for edge-vacancy disorder only (100 configurations average, $P_v = 0.125\%$ over 1 μm). Conductance $\langle G \rangle_{\Delta E}$ is averaged over both an energy interval ΔE and over three edge-vacancy configurations, where $\Delta E = 2.5 \times 10^{-3} t$.

configurations. We have also performed the average of G for a given disorder configuration over a small energy interval. Both averages have demonstrated the robustness of the nodal physics found in this work.

Effects of disorder on our Fano-peak results due to random edge vacancies are presented in Fig. 7. The edge vacancies are distributed on the AGNR sites along its two edges with an occupancy $P_v = 0.125\%$, and over a length $L_0 \sim 1\ \mu$m. An edge vacancy is described by an on-site potential $V_0 \to \infty$. The ensemble average over 100 edge-vacancy configurations gives us $\langle G \rangle$ (solid curves) in the presence of an adsorbate pair, and the background conductance $\langle G_{BG} \rangle$ (grey curves) in the absence of any adsorbate. The adsorbate pairs in Fig. 7 are the same as those in Figs 6(d) and 6(e), where their conductances are plotted again in Fig. 7 as G_p (dotted curves) for comparison. Disorder effects of G on an adsorbate pair for F is presented in Figs. 7(a)– 7(c), and for OH is in Figs. 7(d)– 7(f).

Figure 7 shows that our Fano results remain significant in the presence of disorder. Equally remarkable is the robustness of the Fano-peak energies against the disorder. Even though the conductance at the Fano peak is no longer of value $2e^2/h$, it manages to rise to the same level as $\langle G_{BG} \rangle$. This is understood from our analysis in Eq. (28). The monotonic decreasing of $\langle G_{BG} \rangle$ to zero as E approaches the Dirac point ($E = 0$) is the symmetric edge-vacancy-induced gap-opening feature [20]. Thus the Fano-peak conductances for F suffer less suppression from disorder than that for OH, due to the farther distance of their Fano-peak energies from the Dirac point. Yet the Fano structures of OH remain significant enough for our purposes here. On the same token, our results should hold for the case of hydrogen-passivated AGNR, due to its small energy-gap opening effect on the metallic AGNR ($|E| \leqslant 0.02t$ for $W = 20$) [43,44]. The recent atomically precise bottom-up fabrication of AGNR [45–47] shows an encouraging trend of achieving low edge-disorder W-AGNR in the near future. The recent development of the STM tip-assisted nanopatterning [48] would provide the exciting adsorbate-maneuvering capability for the experimental implementation of this study.

The ensemble averaged $\langle G \rangle$ in Fig. 7 has taken 100 random edge-vacancy configurations into consideration. It is legitimate to see how this large demand of configurations could be reduced for the realization in an experiment. Making use of the mesoscopic characteristics of the quantum transport [36], we introduce, for a given edge-vacancy configuration, an energy average of G over a small energy interval ΔE. For our purpose here, we choose $\Delta E = 2.5 \times 10^{-3}\, t$. We show, in Fig. 8, that this energy average procedure has dramatically reduced the demand on the configuration size by using only three randomly chosen configurations. With merely three configurations, we see that the Fano characteristics in $\langle G \rangle_{\Delta E}$ are very clear in Figs. 8(a), 8(b), 8(d), and 8(f). As for Figs. 8(c) and 8(e), the $\langle G \rangle_{\Delta E}$ already shows sharp-change characteristics at the positions of the Fano peaks (guided by the G_p curves). This rapid converging to the Fano characteristics by energy averaging is an impressive demonstration of the mesoscopic physics [36].

We have established that the Fano structures of an adsorbate pair (a nodal and non-nodal pair) is robust against weak edge-vacancy disorder. The effect of other adsorbates on the adsorbate pair is addressed in the following. Figure 5 has shown that when these other adsorbates are nodal, the Fano structures of the adsorbate pair are not suppressed. On the other hand, when these other adsorbates are non-nodal, they could affect the Fano structures. In the low adsorbate

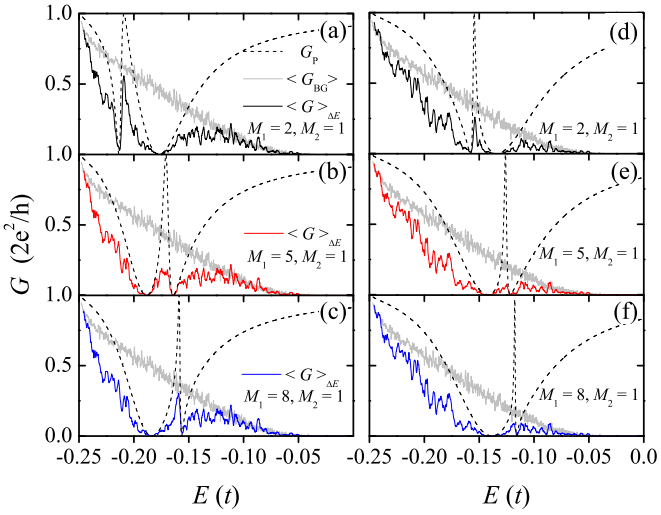

FIG. 9. (Color online) Effects of an additional random adsorbate A3 on the Fano structures of an adsorbate pair in the presence of edge-vacancy disorder. The adsorbate pair, located at M_1 and M_2, are separated by $L = 3$. Adsorbates are F in (a)–(c), and OH in (d)–(f). A3 locates randomly over M and A3-pair L separation is within a 0.5-μm range. $\langle G \rangle_{\Delta E}$ is defined as in Fig. 8, but for five configurations of edge vacancies and A3.

concentration regime, we consider the effects of an additional random adsorbate on the Fano structures of the adsorbate pair in the presence of edge-vacancy disorder. This is presented in Fig. 9. Adsorbates are F in (a)–(c), and OH in (d)–(f). For the $\langle G \rangle_{\Delta E}$, we have included five random configurations of the additional adsorbate and the edge vacancies. The additional adsorbate locates randomly over all possible M sites and over a longitudinal distance of 1.0 μm. This is equivalent to an adsorbate concentration $P_a \approx 3.1 \times 10^{-3}\%$ for the adsorbate system. The edge-vacancy concentration $P_v \approx 0.125\%$ is the same as in Fig. 8. Overall, Fig. 9 shows that the Fano structures remain evident even though there are signs of suppression. In particular, they are quite robust for Figs. 9(a)– 9(d), and recognizable (guided by the G_p curves) for Figs. 9(e) and 9(f).

IV. CONCLUSION

In conclusion, using AGNR as a platform, we have performed investigation on the concept of nodal physics and the possible physical objects that it can lead to. Specifically, we have pointed out that nodal adsorbate induces a bound state in metallic AGNRs, that the bound-state energy is adsorbate dependent, and that it is robust against weak disorder. It is revealed in Fano resonances via a non-nodal adsorbate, which greatly enhanced the energy resolution. It allows adsorbate recognition, when its Hückel parameters are known, and Hückel parameters probing, when the adsorbate is known. Finally, the generic nature of this work should encourage further research on nodal physics in other physical systems.

ACKNOWLEDGMENTS

This work was supported by Ministry of Science and Technology, Taiwan (Contract No. NSC 102-2112-M-009-005-MY3), NCTS Taiwan, and a MOE-ATU grant.

[1] A. H. Castro Neto, F. Guinea, N. M. R. Peres, K. S. Novoselov, and A. K. Geim, Rev. Mod. Phys. **81**, 109 (2009).
[2] K. S. Novoselov, Rev. Mod. Phys. **83**, 837 (2011).
[3] V. Barone, O. Hod, and G. E. Scuseria, Nano Lett. **6**, 2748 (2006).
[4] Y. M. Lin, V. Perebeinos, Z. H. Chen, and P. Avouris, Phys. Rev. B **78**, 161409(R) (2008).
[5] M. Y. Han, J. C. Brant, and P. Kim, Phys. Rev. Lett. **104**, 056801 (2010).
[6] L. Jiao, X. Wang, G. Diankov, H. Wang, and H. Dai, Nat. Nanotechnol. **5**, 321 (2010).
[7] L. Liao, J. Bai, R. Cheng, Y. C. Lin, S. Jiang, Y. Huang, and X. Duan, Nano Lett. **10**, 1917 (2010).
[8] X. Wang, Y. Ouyang, L. Jiao, H. Wang, L. Xie, J. Wu, J. Guo, and H. Dai, Nat. Nanotechnol. **6**, 563 (2011).
[9] A. Felten, A. Eckmann, J.-J. Pireaux, R. Krupke, and C. Casiraghi, Nanotechnology **24**, 355705 (2013).
[10] K. Wakabayashi, Phys. Rev. B **64**, 125428 (2001).
[11] D. A. Areshkin, D. Gunlycke, and C. T. White, Nano Lett. **7**, 204 (2007).
[12] E. R. Mucciolo, A. H. Castro Neto, and C. H. Lewenkopf, Phys. Rev. B **79**, 075407 (2009).
[13] B. Biel, X. Blase, F. Triozon, and S. Roche, Phys. Rev. Lett. **102**, 096803 (2009).
[14] J. Y. Yan, P. Zhang, B. Sun, H. Z. Lu, Z. G. Wang, S. Q. Duan, and X. G. Zhao, Phys. Rev. B **79**, 115403 (2009).
[15] A. López-Bezanilla, F. Triozon, and S. Roche, Nano Lett. **9**, 2537 (2009).
[16] S. Ihnatsenka and G. Kirczenow, Phys. Rev. B **80**, 201407(R) (2009).
[17] I. Deretzis, G. Fiori, G. Iannaccone, and A. La Magna, Phys. Rev. B **81**, 085427 (2010).
[18] D. A. Bahamon, A. L. C. Pereira, and P. A. Schulz, Phys. Rev. B **82**, 165438 (2010).
[19] K. Saloriutta, Y. Hancock, A. Karkkainen, L. Karkkainen, M. J. Puska, and A.-P. Jauho, Phys. Rev. B **83**, 205125 (2011).
[20] S. Ihnatsenka and G. Kirczenow, Phys. Rev. B **83**, 245442 (2011).
[21] K. Saloriutta, A. Uppstu, A. Harju, and M. J. Puska, Phys. Rev. B **86**, 235417 (2012).
[22] A. Orlof, J. Ruseckas, and I. V. Zozoulenko, Phys. Rev. B **88**, 125409 (2013).
[23] J. Wilhelm, M. Walz, and F. Evers, Phys. Rev. B **89**, 195406 (2014).
[24] L. Brey and H. A. Fertig, Phys. Rev. B **73**, 235411 (2006).
[25] The nodal behavior in AGNR is shown in Fig. 6(a) of Ref. [24] for $L = 25a_0$ AGNR (or $W = 50a$ AGNR in this work), where the magnitude square of the gapless-subband wave function for site-B carbon atoms is plotted along the width of the AGNR. The nodal sites are exhibited by zeros in the wave function.
[26] F. Schedin, A. K. Geim, S. V. Morozov, E. W. Hill, P. Blake, M. I. Katsnelson, and K. S. Novoselov, Nat. Mater. **6**, 652 (2007).

[27] T. O. Wehling, K. S. Novoselov, S. V. Morozov, E. E. Vdovin, M. I. Katsnelson, A. K. Geim, and A. I. Lichtenstein, Nano Lett. **8**, 173 (2008).
[28] Y. P. Dan, Y. Lu, N. J. Kybert, Z. T. Luo, and A. T. C. Johnson, Nano Lett. **9**, 1472 (2009).
[29] P. L. Levesque, S. S. Sabri, C. M. Aquirre, J. Guillemette, M. Siaj, P. Desjardins, T. Szkopek, and R. Martel, Nano Lett. **11**, 132 (2011).
[30] W. J. Yuan and G. Q. Shi, J. Mater. Chem. A **1**, 10078 (2013), and the references cited therein.
[31] V. G. Kravets, F. Schedin, R. Jalil, L. Britnell, R. V. Gorbachev, D. Ansell, B. Thackray, K. S. Novoselov, A. K. Geim, A. V. Kabashin, and A. N. Gigorenko, Nat. Mater. **12**, 304 (2013).
[32] A. J. Haes and R. P. Van Duyne, J. Am. Chem. Soc. **124**, 10596 (2002).
[33] S. Zou, N. Janel, and G. C. Schatz, J. Chem. Phys. **120**, 10871 (2004); V. A. Markel, J. Phys. B **38**, L115 (2005); V. G. Kravets, F. Schedin, and A. N. Grigorenko, Phys. Rev. Lett. **101**, 087403 (2008); B. Auguie and W. L. Barnes, *ibid*. **101**, 143902 (2008); Y. Chu, E. Schonbrun, T. Yang, and K. B. Cozier, Appl. Phys. Lett. **93**, 181108 (2008).
[34] A. N. Grigorenko, P. I. Nikitin, and A. V. Kabashin, Appl. Phys. Lett. **75**, 3917 (1999).
[35] A. E. Miroshnichenko, S. Flach, and Y. S. Kivshar, Rev. Mod. Phys. **82**, 2257 (2010).
[36] C. W. J. Beenakker and H. van Houten, *Quantum Transport in Semiconductor Nanostructures*, Solid State Physics, edited by H. Ehrenreich and D. Turnbull (Academic, New York, 1991), Vol. 44, p. 1.
[37] M. Fujita, K. Wakabayashi, K. Nakada, and K. Kusakabe, J. Phys. Soc. Jpn. **65**, 1920 (1996).
[38] M. Ezawa, Phys. Rev. B **73**, 045432 (2006).
[39] C. H. Chiu and C. S. Chu, Phys. Rev. B **85**, 155444 (2012).
[40] Our analytic evaluation of the reduced Green's function uses the conventional choice of unit cells for graphene and is a different calculation from that in Ref. [22]. The same results for the case of a single vacancy in an AGNR [Fig. 5(c) in Ref. [22]] are obtained by both calculations.
[41] F. Ducastelle, Phys. Rev. B **88**, 075413 (2013).
[42] T. Welhing, A. Balatsky, M. I. Katsnelson, A. Lichtenstein, K. Scharnberg, and R. Wiesendanger, Phys. Rev. B **75**, 125425 (2007).
[43] Y. W. Son, M. L. Cohen, and S. G. Louie, Phys. Rev. Lett. **97**, 216803 (2006).
[44] Y. H. Lu, R. Q. Wu, L. Shen, M. Yang, Z. D. Sha, Y. Q. Cai, P. M. He, and Y. P. Feng, Appl. Phys. Lett. **94**, 122111 (2009).
[45] J. M. Cai, P. Ruffieux, R. Jaafar, M. Bieri, T. Braun, S. Blankenburg, M. Muoth, A. P. Seitsonen, M. Saleh, X. L. Feng, K. Müllen, and R. Fasel, Nature (London) **466**, 470 (2010).
[46] H. Huang, D. Wei, J. Sun, S. L. Wong, Y. P. Feng, A. H. Castro Neto, and A. T. S. Wee, Sci. Rep. **2**, 983 (2012).
[47] Y. C. Chen, D. G. de Oteyza, Z. Pedramrazi, C. Chen, F. R. Fischer, and M. F. Crommie, ACS Nano **7**, 6123 (2013).
[48] R. Balog, B. Jørgensen, J. Wells, E. Lægsgaard, P. Hofmamm, F. Besenbacher, and L. Hornekær, J. Am. Chem. Soc. **131**, 8744 (2009).